

Drude Dispersion in the Transmission Line Modeling of Bulk Absorbers at Sub-mm Wave Frequencies

A Tool for Absorber Optimization

van Schelven, Ralph Matthijs; Fiorellini Bernardis, Arturo; Sberna, Paolo; Neto, Andrea

DOI

[10.1109/MAP.2021.3073092](https://doi.org/10.1109/MAP.2021.3073092)

Publication date

2021

Document Version

Final published version

Published in

IEEE Antennas and Propagation Magazine

Citation (APA)

van Schelven, R. M., Fiorellini Bernardis, A., Sberna, P., & Neto, A. (2021). Drude Dispersion in the Transmission Line Modeling of Bulk Absorbers at Sub-mm Wave Frequencies: A Tool for Absorber Optimization. *IEEE Antennas and Propagation Magazine*, 64 (2022)(1), 50-60. Article 9428649. <https://doi.org/10.1109/MAP.2021.3073092>

Important note

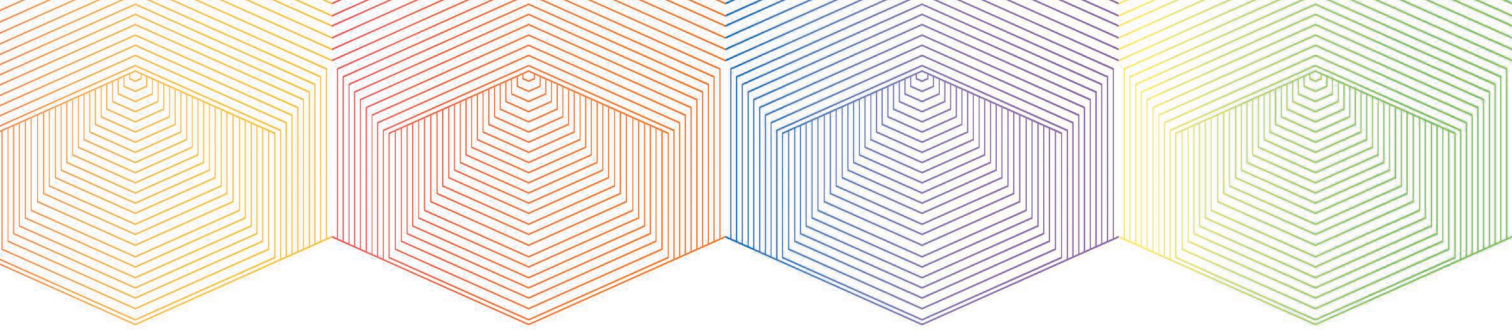
To cite this publication, please use the final published version (if applicable). Please check the document version above.

Copyright

Other than for strictly personal use, it is not permitted to download, forward or distribute the text or part of it, without the consent of the author(s) and/or copyright holder(s), unless the work is under an open content license such as Creative Commons.

Takedown policy

Please contact us and provide details if you believe this document breaches copyrights. We will remove access to the work immediately and investigate your claim.



Ralph M. van Schelven, Arturo Fiorellini Bernardis, Paolo Sberna, and Andrea Neto

Drude Dispersion in the Transmission Line Modeling of Bulk Absorbers at Sub-mm Wave Frequencies

A tool for absorber optimization.

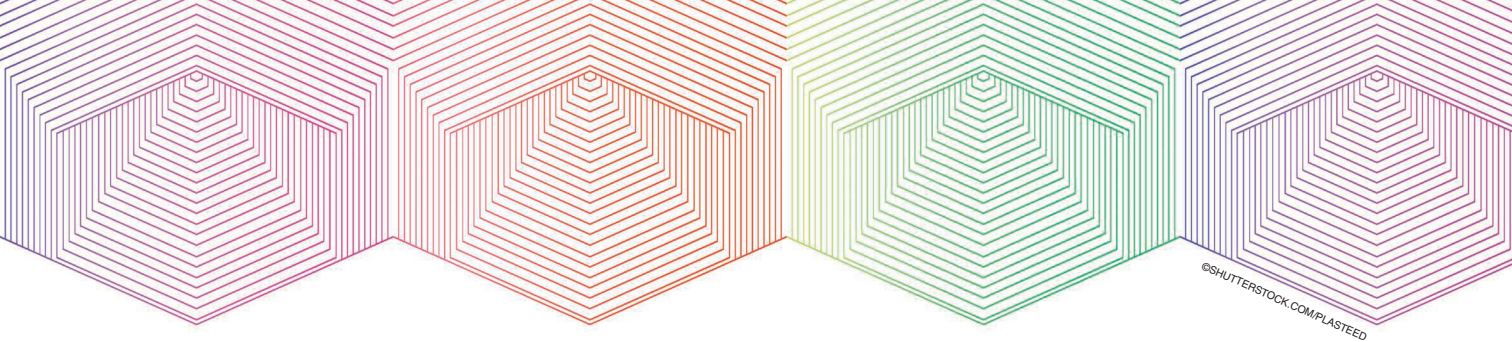
Semiconductor (SC)-based bulk absorbers operating in the (sub-) THz range are discussed. The conductivities of the bulk media are described by the Drude model for electron gas where the electron density is controlled. The Drude model predicts the existence of two frequencies of interest: one associated with the scattering time of the electrons and a second associated with the plasma frequency. The dimensions of the absorbers for a specific frequency range can be minimized by tuning the doping levels. Eventually, the maximum ohmic absorption from a bulk material is achieved when the real part of the characteristic impedance of the absorber is matched to the one of the surrounding medium and the imaginary

part of the characteristic impedance is high so that the power entering the material is actually transformed in heat. Using a classic transmission line representation, a matching layer is introduced to further increase the absorption capabilities of an SC slab. Measurements using a time-domain spectroscopy (TDS) system show the increased accuracy of the Drude model compared to the quasi-static approximation of the conductivity. The transmission line representation in combination with the Drude model proves to be a simple and accurate tool for integrated antenna front-end design and absorber optimization.

DRUDE MODEL PREDICTIONS

The Drude theory for conduction electrons is a fairly accurate description of the electromagnetic (EM) waves' dispersion in metals [1] whose typical resistivities are lower than

Digital Object Identifier 10.1109/MAP.2021.3073092
Date of current version: 11 May 2021



$10^{-4} \Omega \text{ cm}$. However, the antennas scientific community often does not consider all of the theory's details since the dependence of the conductivity of metals on frequency starts to become significant at frequencies much higher than the upper limit of the antennas' working frequency range (i.e., hundreds of GHz). Metals up to 5 THz can be considered very good conductors, amenable to the low-loss simplifications assumed by Leontovich [2].

However, for mildly doped SCs whose typical resistivity falls between 1 and $100 \Omega \text{ cm}$, the Drude model predicts a strong frequency dependence of the conductivity and dielectric constant already in the GHz range. The dispersion properties of SCs were observed with increasing interest since the fabrication of the first silicon (Si) and germanium devices (diodes, bipolar transistors, etc.). Later, the first models for the high-frequency (>100-GHz) properties of these devices were developed beginning in the mid-1960s [3]. In particular, the Drude model was proven to be fundamental for the explanation of the high-frequency diode response as a function of the spreading resistance [4]. Moreover, it was not before 1978, the high-frequency cutoff of Schottky diodes was understood, again thanks to the Drude theory of free charge carriers in SCs [5].

During the 1990s, significant technological breakthroughs in THz TDS [6] allowed for the accurate measurement of SCs' free charge carriers' scattering time, electrical mobility, and effective mass. The experimental results reported in [6]–[8] also demonstrated that the Drude model, despite its simplicity, describes these conduction parameters well for SCs, such as Si, in the GHz and THz range. For specific reading, comprehensive reviews on SC dispersion can be found in [9], [10]. To overcome some inaccuracies and limitations of the Drude theory for SCs, numerical approaches based on Monte Carlo simulations, Maxwell equations, and molecular dynamics have been presented in [11]. However, this kind of complex methodology resulted in less than 10% more accuracy for the determination of the frequency-dependent complex conductivity of Si. Hence, the Drude theory remains the simplest classical model that can predict SCs' dispersion properties with minimal computational efforts, allowing the fast engineering of SC-based components for antenna systems and imagers.

For historical reasons, all of Drude theory's aspects and consequences, widely studied by the physicist and time-domain communities, have not yet received proper attention from the microwave and THz engineering communities. For example, in the modeling of the state of the art of CMOS integrated detectors (one pixel of which could be as presented in Figure 1) and imaging arrays [12], the material's dielectric constant has been assumed to be frequency independent. Although the

consequences of assuming the conductivity is frequency independent are negligible for some highly resistive materials, such as the material considered in [13], for other materials, the over-estimation of the ohmic losses is very significant [14].

Moreover, it appears that SC composites have not yet been exploited in the design of absorbers. Bulk absorbers in the THz regime could be simply fabricated by Si micromachining and deep reactive-ion etching. High-resolution imaging in the THz band, [12], [15]–[17] for instance, is a technological field in which arrays of antenna-coupled dielectric lenses are often adopted. Each lens corresponds to a specific observation direction, and the mutual coupling between the feeds of different lenses must be avoided. The mutual coupling can be diminished by selectively increasing the conductivity of specific lateral portions of the lenses to render them opaque, as displayed in Figure 2.

When complying with stringent volume requirements, the fine-tuning of the parameters of the SC slabs leads to significant ohmic losses, which can be characterized by equivalent transmission lines. These losses imply characteristic impedances whose imaginary parts are comparable to the real parts. These lines are not usually addressed in the microwave community, and they require a heuristic approach to the design as there are no well-known design principles.

ANALYSIS OF THE CONDUCTOR USING THE DRUDE MODEL

The most important characteristics of the Drude model will be briefly summarized in this section to provide the reader with a complete view and to introduce essential variables and terminology used in this article. The effective parameters from the Drude model as a function of the frequency are discussed with a focus on bulk metals (specifically gold).

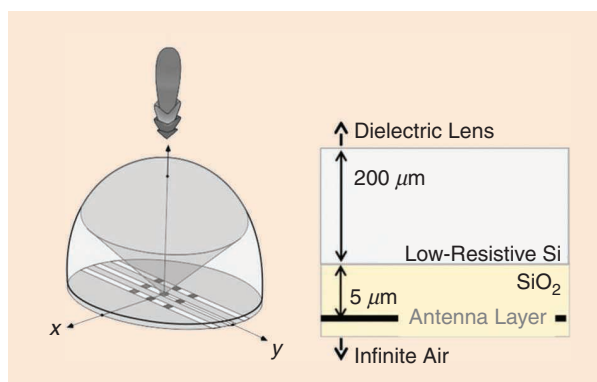


FIGURE 1. An example of stratification consisting of an antenna and a dielectric lens, separated by a thin layer of low-resistivity Si.

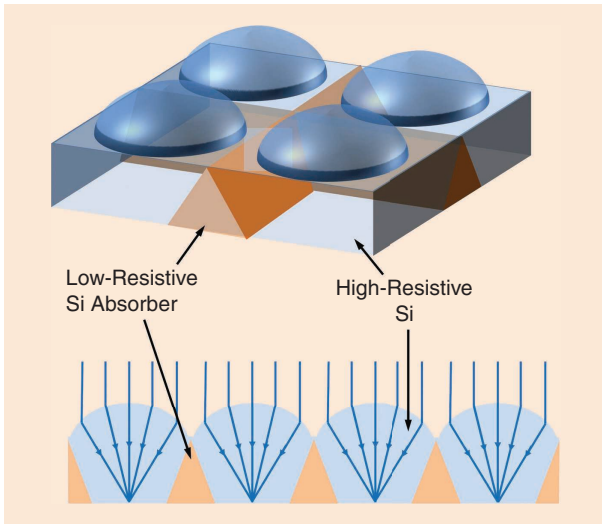


FIGURE 2. An on-chip lens array made of high-resistive Si. Locally increasing the doping levels for maximum absorption can reduce surface wave-propagation in the chip.

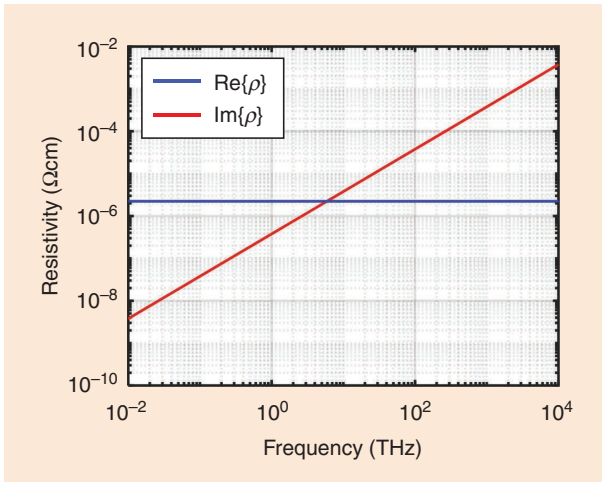


FIGURE 3. The resistivity of gold as a function of the frequency calculated using the given parameters.

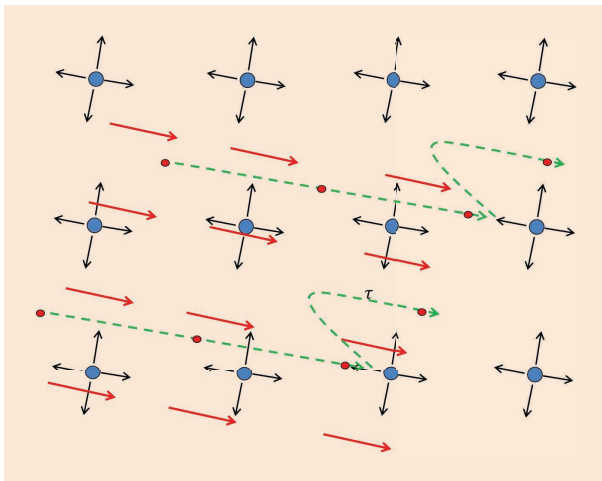


FIGURE 4. The free electrons (red dots) are accelerated by a low-frequency electric field (red arrows) until they hit a metal ion (blue dots), which, in turn, is accelerated.

In the quasi-static limit, the conductivity of a metal or an SC can be approximated as

$$\sigma_{qs} = \frac{ne^2\tau}{m_e}, \quad (1)$$

where n is the electron density, $e = 1.6 \times 10^{-19}$ C is the charge of an electron, and $m_e = 9.1 \times 10^{-31}$ kg is the mass of a free electron. The scattering time, τ , characterizes the electron gas, and, in the case of a metal, it is in the order of femto seconds (27 fs for gold at room temperature).

The model predicts a linear frequency-dependent resistivity as

$$\rho(\omega) = \rho_{qs}(1 + j\omega\tau), \quad (2)$$

where $\rho_{qs} = 1/\sigma_{qs}$, and both σ_{qs} and τ have been provided in (1). As a specific case, the resistivity of gold, calculated using the Drude model, at 300 K, is presented in Figure 3. The electron density is $n = 5.9 \times 10^{28}$ electrons/m³. It is seen that, at very low frequency, the resistivity is mostly real. The Drude model introduces a frequency dependence for the conductivity of the metal, describing the bulk material as an ion sea, with free electrons. The free electrons are accelerated by the presence of an electric field and hit the metal ions, as illustrated in Figure 4. When these hits occur, kinetic energy is transferred to the ions, which are accelerated, and, as a consequence, heat is generated. In a first-order approximation, the average time, τ , between the successive hits of electrons and the ion sea does not depend on the electric field. Instead, it depends on the effective scattering surface of the ions, which is a function of the temperature via the average energy of the ions. Significant changes in the resistivity occur as the frequency of the EM wave propagating in the metal increases. At the transition frequency $f = f_\tau = 1/(2\pi\tau)$, which corresponds to 6 THz for gold, the imaginary part of the resistivity becomes as large as the real part. This corresponds to the notion that for frequencies higher than f_τ , the electric field changes sign with a period shorter than τ . Accordingly, within the time interval τ the electrons are accelerated in alternating opposite directions. For this reason, the electrons do not discharge all of the kinetic energy that they acquired into the ion sea. A pictorial view of the average electron accelerated by a high-frequency electric field is presented in Figure 5.

From (2), the frequency-dependent conductivity is

$$\sigma(\omega) = \frac{\sigma_{qs}}{1 + j\omega\tau} = \frac{\sigma_{qs}}{1 + \omega^2\tau^2} - j\frac{\sigma_{qs}\omega\tau}{1 + \omega^2\tau^2}. \quad (3)$$

The introduction of (3) in Maxwell's equations provides the effective dielectric constant

$$\epsilon_{\text{eff}}(\omega) = \epsilon_0 \epsilon_{r,\text{eff}} = \epsilon_0 \epsilon_{r\infty} \left(1 - \frac{j\sigma(\omega)}{\omega \epsilon_{r\infty} \epsilon_0} \right). \quad (4)$$

The effective dielectric constant presents both a real and an imaginary part, which can be isolated after introducing the plasma frequency as [18]:

$$\omega_p^2 = \frac{ne^2}{\epsilon_{r\infty} \epsilon_0 m_e}. \quad (5)$$

One finds

$$\begin{aligned} \epsilon_{r,\text{eff}}(\omega) = \epsilon_{r\infty} \left[1 - \omega_p^2 \tau^2 \left(\frac{1}{1 + \omega^2 \tau^2} \right) \right] \\ - j \epsilon_{r\infty} \omega_p^2 \frac{\tau^2}{\tau \omega} \left(\frac{1}{1 + \omega^2 \tau^2} \right). \end{aligned} \quad (6)$$

The absolute values of the real and imaginary parts of the effective relative dielectric constant are plotted in Figure 6 again for the case of gold, calculated using the given parameters ($\epsilon_{r\infty} = 1$). The term in (6) within the square parenthesis expresses the real part of the effective relative dielectric constant. Since $\omega_p^2 \tau^2 \approx 1.6 \times 10^5$ for gold at room temperature, it is apparent that for frequencies lower than the plasma frequency the real part of the effective dielectric constant is negative.

A similar transition to the one that was observed in the resistivity can be observed in the equivalent relative dielectric constant. For frequencies lower than f_r , the imaginary part of the effective relative dielectric constant is much larger than the real part. Also, at extremely high frequencies ($f > f_p$, $f_p = \omega_p/2\pi$), gold (as all metals) becomes transparent.

The propagation constant also shows a signature associated to the f_r transition. The propagation constant for gold, calculated using the Drude model, is plotted in Figure 7 with frequencies varied both in linear and in logarithmic scale. For frequencies below 2,200 THz propagation in gold is highly attenuated. However, on a logarithmic scale, it is apparent that from dc to the mentioned $f_r = 6$ THz the amplitude of the real part of the propagation constant increases in the same way as the amplitude of the imaginary part. At $f_r = 6$ THz the real part of the propagation constant reaches a maximum value and then decreases while the imaginary part saturates at approximately 20 THz.

The transition that characterizes the propagation and attenuation constant corresponds to the change in the dominant mechanism of attenuation for the EM waves in the metal:

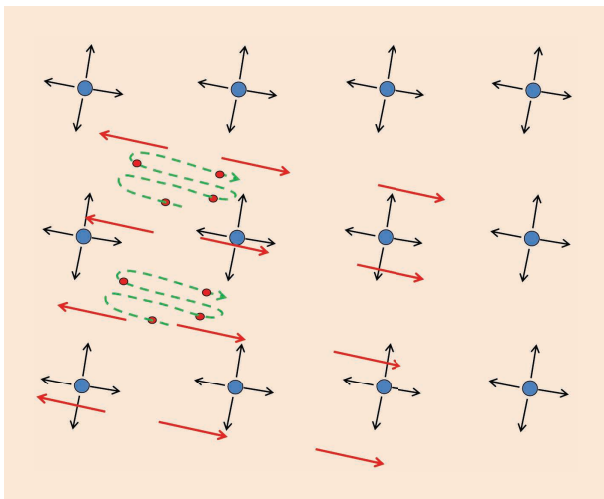


FIGURE 5. The free electrons (red dots) are accelerated by a high-frequency electric field (red arrows). The direction of the electric field changes sign before the electrons hit an ion (blue dots), and the electrons oscillate without transferring energy to the ions.

At low frequencies there are ohmic losses corresponding to the transformation of EM energy into kinetic energy while at higher frequencies there is attenuation with minimal phase

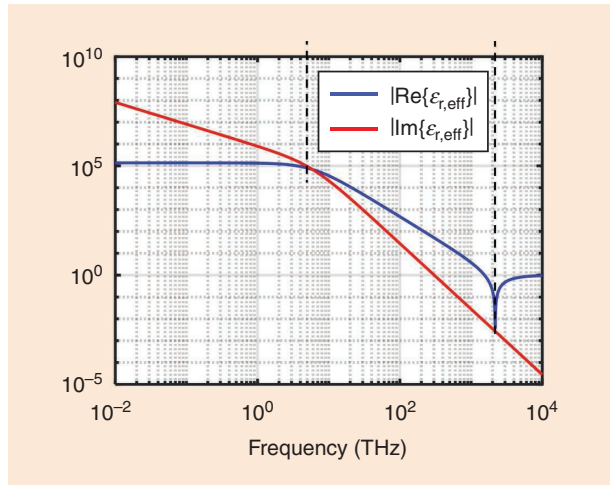


FIGURE 6. The absolute value of the real and imaginary parts of the effective relative permittivity of gold, calculated using the given parameters. Both the real and imaginary parts are negative for frequencies lower than the plasma frequency.

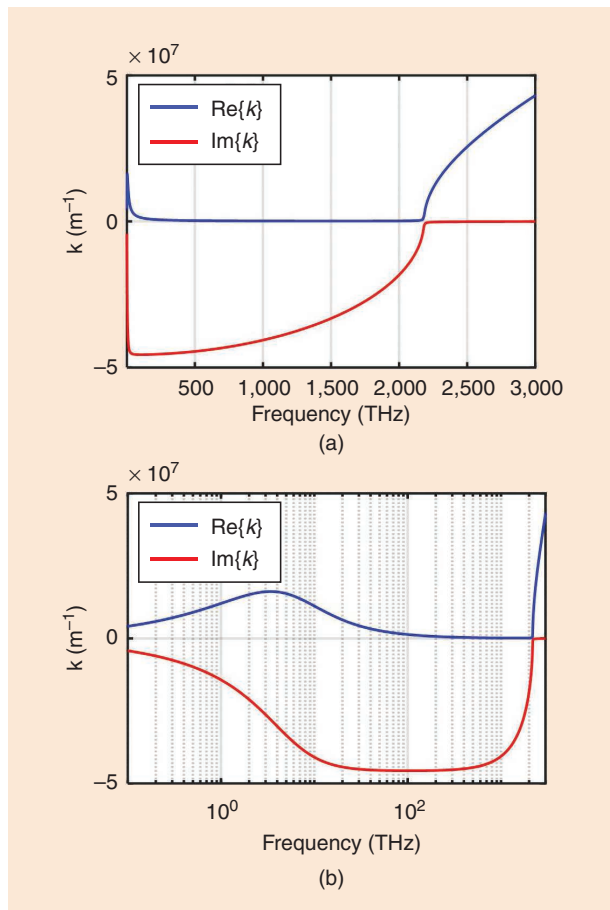


FIGURE 7. The propagation constant of an EM wave within gold, calculated using the given parameters. (a) Frequency on a linear scale. (b) Frequency on a logarithmic scale.

progression. The electron density in the metal is very high, and as the electrons are excited by an incident wave they radiate a scattered field, which opposes the propagation of waves (similarly to what happens in a waveguide in cutoff). As long as the average distances between the electrons are small in terms of the wavelength the scattering destructively interferes with progressive waves in the metal. As the frequency increases, the electrons become too massive to respond with an acceleration to the force impressed by the electric field before it changes sign. Since the electrons are less accelerated, they also do not radiate the scattered field. Therefore, the total field in the metal is only represented by the incident field that can propagate in the metal unobstructed. The specific frequency at which this

All of Drude theory's aspects and consequences, widely studied by the physicist and time-domain communities, have not yet received proper attention from the microwave and THz engineering communities.

happens, f_p , depends on the electron density and the effective mass of the electrons. Mathematically, this condition is represented by the real part of the effective dielectric constant rising higher than zero, i.e., $1 - \omega_p^2 \tau^2 / (1 + \omega^2 \tau^2) > 0$, which happens as the frequency increases to values higher than the plasma frequency.

Another interesting parameter is the characteristic impedance of the gold calculated using the Drude model, which is illustrated in Figure 8. The impedance tends to $\zeta_0 \approx 377 \Omega$ for frequencies much higher than the plasma frequency of the metal, it undergoes a resonance at the plasma frequency, and it is mostly imaginary for

lower frequencies. However, a zoomed view of the impedance curves at low frequencies [Figure 8(b)] shows that for frequencies below 1 THz the real and imaginary parts of the impedance tend to be equal. Real and imaginary parts having the same value is the signature of the “good conductor” behavior on which the Leontovich [2] approximation for losses is built.

SC DISPERSION

For doped bulk SC materials, the quasi-static conductivity can be approximated using (1). Here, we are neglecting the hole conductivity, which is negligible for n-doped SC materials. For SCs, an equivalent electron mass is used to account for the diminished inertia of electrons embedded in a periodic lattice potential: $m_{e,si} = 0.29 m_e$ for Si [6]. The scattering time τ for Si is in the order of a few ps, depending on the doping and the temperature. The scattering time is found as

$$\tau = \frac{m_{si}}{e} \mu, \quad (7)$$

where the mobility μ is at $T = 300$ K, equal to [19]:

$$\mu = \mu_{\min} + \frac{\mu_{\max} - \mu_{\min}}{1 + \left(\frac{n}{N_{\text{ref},1}}\right)^{\alpha_1}} - \frac{\mu_1}{1 + \left(\frac{N_{\text{ref},2}}{n}\right)^{\alpha_2}}. \quad (8)$$

The several parameters in (8) are based on experimental data, and the values are: $\mu_{\min} = 6.85 \times 10^{-3} \text{ m}^2 \text{ V}^{-1} \text{ s}^{-1}$, $\mu_{\max} = 0.1414 \text{ m}^2 \text{ V}^{-1} \text{ s}^{-1}$, $\mu_1 = 5.61 \times 10^{-3} \text{ m}^2 \text{ V}^{-1} \text{ s}^{-1}$, $N_{\text{ref},1} = 9.20 \times 10^{22} \text{ m}^{-3}$, $N_{\text{ref},2} = 3.41 \times 10^{26} \text{ m}^{-3}$, $\alpha_1 = 0.711$, and $\alpha_2 = 1.98$. For SC materials, the transition frequencies, f_τ , are in the range of a few hundred GHz. The plasma frequencies can also be in this frequency range depending on the doping levels. Therefore, both of these frequencies should be reasons for attention, specifically from mm- and sub-mmWave front-end designers.

Similar to the case of gold, the effective relative permittivity of the SC can be calculated as a function of frequency from

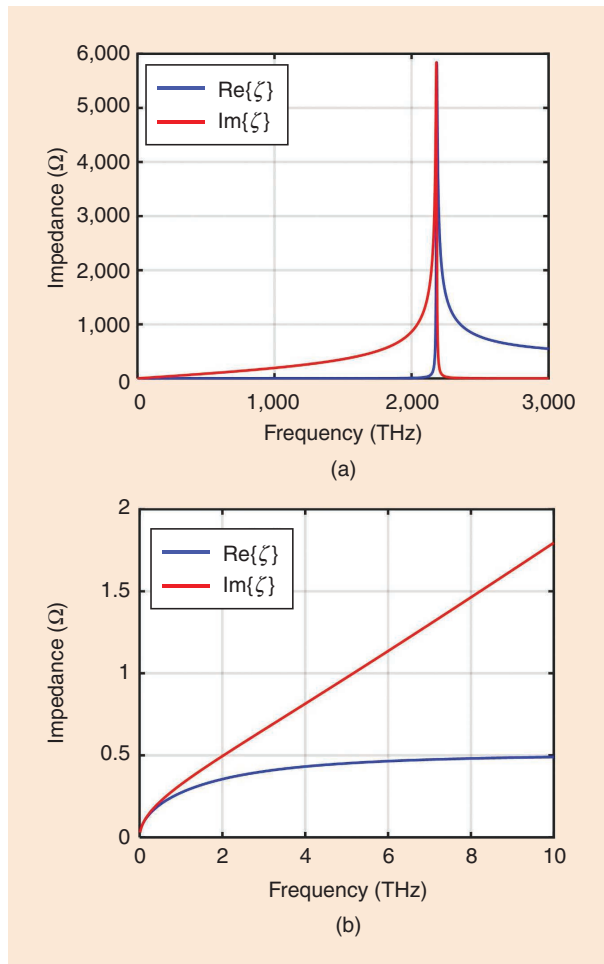


FIGURE 8. The characteristic impedance of gold, calculated using the given parameters. (a) Complete spectrum under consideration. (b) Zoomed in on low frequencies.

the Drude model using (6) so that the characteristic impedance of the SC and its propagation constant are expressed as $\zeta = \zeta_0 / \sqrt{\epsilon_{r,\text{eff}}}$ and $k = k_0 \sqrt{\epsilon_{r,\text{eff}}}$, respectively. Figure 9 presents the dispersion curves of plane waves propagating in gold [Figure 9(a)] and in doped Si [Figure 9(b)], calculated using the Drude model and the appropriate parameter values. The propagation constants normalized to the propagation constant of free space, k_0 , (for gold) and to the propagation constant of undoped Si, $k_{\text{host}} = k_0 \sqrt{\epsilon_{r,\infty}}$, (for Si) are shown as functions of the frequency. The propagation constant of gold undergoes a very drastic transition after $f_p = 2,200$ THz as waves are actually allowed to propagate without significant attenuation for frequencies higher than f_p . The case of Si presents a more complex dispersion. The plasma frequency in SCs largely depends on the doping levels, and, accordingly, the dispersive properties can be designed to meet certain requirements. In the case presented in Figure 9(b), four different levels of doping are considered. The parametrization refers to $n = n_p = (\epsilon_{r,\infty} \epsilon_0 m_{e,\text{Si}}) / (\tau_{\text{Si}}^2 e^2) = 8.8 \times 10^{21} \text{ m}^{-3}$. This doping is such that $f_p = f_\tau$ and corresponds to $\rho_{\text{qs}} = 0.6 \Omega\text{cm}$. These orders of doping levels are common in Si wafers used in electronic circuits. The dopings of Figure 9(b) correspond to $n = n_p/5$, $n = n_p$, $n = 5n_p$, and $n = 25n_p$. The lower doping

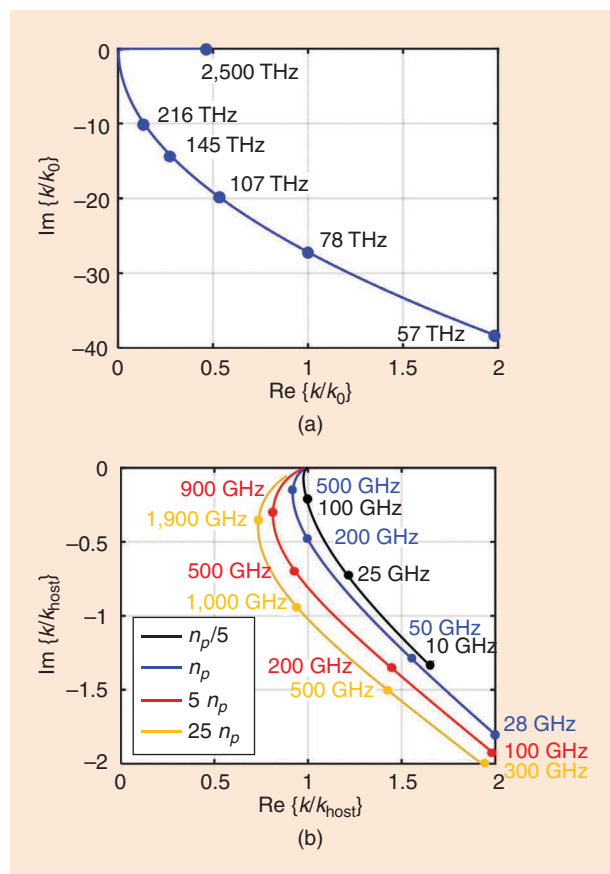


FIGURE 9. The dispersion of the propagation constant, calculated using the given parameters, in the complex plane. (a) In the case of gold. (b) In the case of SCs with varying doping levels. Several frequency points along the different curves are indicated.

levels imply lower dispersion. However, for higher dopings, the frequency dependence of the propagation constant is stronger. From this figure, one can anticipate that significant freedom in the design of front ends at sub-THz frequencies can be obtained by finely controlling the electron doping levels in Si.

IMPEDANCES OF LOW-RESISTIVITY SILICON

Arguably, the most important property of a material for an EM engineer is its characteristic impedance. It relates the electric and magnetic field of a plane wave traveling in a bulk medium and is routinely introduced in transmission line tools to describe the interaction of waves with the finiteness of the structures. The superposition of multiple reflections in slabs is well-understood in the TDS community [6]. However, the representation of the total fields via equivalent transmission lines is much less common there than it is in the electrical engineering community. For this reason, to the authors' knowledge, the characteristic impedance of a bulk SC cannot be found in published literature.

The resistivity of doped Si as calculated using the Drude model with $n = n_p$ is displayed in Figure 10(a). The same behavior as what happens with the resistivity of gold is seen,

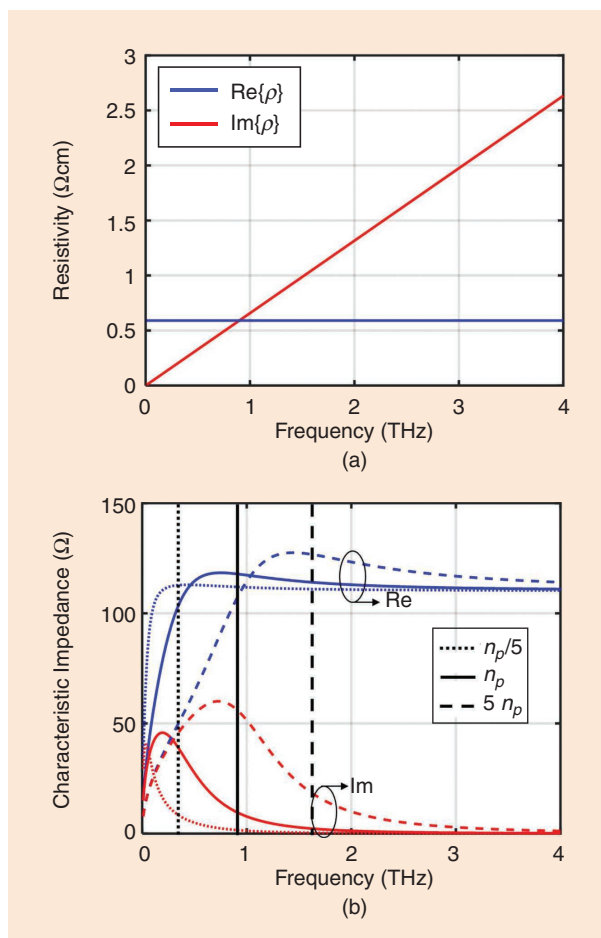


FIGURE 10. (a) The resistivity of doped Si ($n_p = 8.8 \times 10^{21} \text{ m}^{-3}$), calculated using the given parameters, as a function of frequency. (b) Characteristic impedance of doped Si, calculated using the given parameters, for three different levels of doping. The plasma frequencies are also indicated.

where the real part is constant as a function of the frequency while the imaginary part grows linearly, reaching the value of the real part at f_r . The characteristic impedance of Si doped with different electron densities is presented in Figure 10(b). The characteristic impedance of doped Si is

$$\zeta(\omega) = \frac{\zeta_0}{\sqrt{\epsilon_{r,\text{eff}}(\omega)}}, \quad (9)$$

where $\epsilon_{r,\text{eff}}(\omega)$ is introduced in (6). After some algebraic steps, (9) is written as

$$\zeta(\omega) = e^{j\pi/4} \sqrt{\frac{\mu_0 \omega}{\sigma_{qs}}} \sqrt{\frac{1 + \omega^2 \tau^2}{1 + j\gamma(\omega)}}, \quad (10)$$

where we introduced

$$\gamma(\omega) = \frac{\omega}{\omega_p^2 \tau} (1 + (\omega^2 - \omega_p^2) \tau^2). \quad (11)$$

In the limit for low frequency, it can be seen that γ goes to zero so that

$$\zeta(\omega \ll \omega_p) = \sqrt{\frac{\mu_0 \omega}{2\sigma_{qs}}} (1 + j), \quad (12)$$

which is recognized as the Leontovich approximation for good conductors. Instead, for very high frequencies (i.e., $\omega \gg \omega_p$), using $\omega_p^2 \tau = \sigma_{qs} / (\epsilon_{r\infty} \epsilon_0)$, we see

$$\zeta(\omega \gg \omega_p) = \frac{\omega \epsilon_{r\infty} \epsilon_0}{\sigma_{qs}} (1 + \omega^2 \tau^2) \quad (13)$$

so that

$$\zeta(\omega \gg \omega_p) = \sqrt{\frac{\mu_0}{\epsilon_{r\infty} \epsilon_0}}. \quad (14)$$

The impedance behavior in the frequency range around ω_p exhibits an interesting behavior. As the frequency grows from very low frequency, both real and imaginary parts (R_{Si} and X_{Si} , respectively) of the impedance rise and show peaks that are close to each other in frequency. The ‘‘Applications in Absorbers and Lens Design’’ section presents that the percentage of incident power absorbed within the SC is maximal at a frequency between the peaks of R_{Si} and X_{Si} .

A better physical understanding of the imaginary part can be understood as follows: Assuming that a plane wave propagates in a positive z -direction and the magnetic field is of zero phase at a given observation point, the corresponding electric field is

$$\vec{e} = \zeta \vec{h} \times \hat{z} = (R_{Si} + jX_{Si}) \vec{h} \times \hat{z}, \quad (15)$$

which presents two components that are 90° phase-shifted. One component is in phase with the magnetic field, $\vec{e} = R_{Si} \vec{h} \times \hat{z}$,

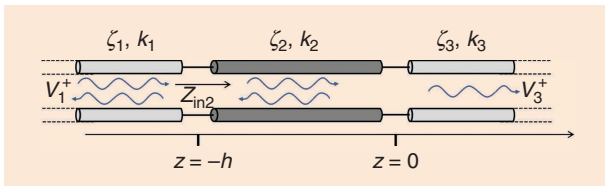


FIGURE 11. The transmission line model representing the absorbing slab surrounded by a lossless host medium.

and, thus, contributes to the real part of the pointing vector along \hat{z} as

$$\text{Re}\{S_z\} = \frac{1}{2} R_{Si} |\vec{h}|^2. \quad (16)$$

The second component is in quadrature to the magnetic field: $\vec{e} = jX_{Si} \vec{h} \times \hat{z}$. This component only contributes to reactive energy transported in the longitudinal direction. However, this same component of the electric field is actually in phase with the flow of electrons in the Si (electric currents) and, thus, directly contributes to losses.

The imaginary part of the characteristic impedance is associated with real power in the form of ohmic losses. It can be observed from Figure 10 that, for increasing frequency, the value of R_{Si} tends to the impedance in the absence of doping while X_{Si} decreases, resulting in lower ohmic losses.

VERIFICATION OF THE MODEL

The Drude model for the dispersion of the SCs in (6) was first validated in [6]. In this section, we present an experimental validation that largely follows the one in [6] by means of state-of-the-art TDS measurement equipment [20] and Si wafers.

The experiment was conducted in the following way: Two photoconductive antennas face each other and are coupled by means of a quasi-optical path consisting of four spherical lenses that focus the field radiated by the transmitting (Tx) antenna onto the receiving (Rx) one. The antennas are excited by a pulsed in-fiber gaussian laser at 1,580 nm, each pulse having a full width at a half-maximum of 100 fs and being repeated at 100 MHz. The Tx antenna is biased to a constant voltage, $V_b = 100$ V, that accelerates the carriers injected by the laser generating the radiating process; the carriers freed in the Rx antenna are accelerated by the incoming THz radiation. The Si wafer is positioned in the middle of the quasi-optical path, the time-domain current induced in the Rx antenna is sampled, and its spectrum is calculated. The spectrum of the induced current on the Rx antenna is calculated both with and without the sample in the quasi-optical path. From these spectra, the dielectric properties of the slab can be extrapolated by knowing the slab’s geometry and location.

Next, we consider an SC slab that is much larger in the transverse directions (i.e., the x - and y -directions) than the width of the beam profile generated by the TDS system. The slab has a finite thickness, h , in z -direction, and it has free space above and below it. The beam profiles can be represented as normally incident plane waves. Thus, the total electric field can be expressed as the product of a voltage, V , and a transverse normalized field unit vector, \hat{e}_t :

$$\vec{E}_t(\vec{r}) = V(z) \hat{e}_t. \quad (17)$$

Resorting to a standard transmission line representation, as illustrated in Figure 11, the voltage distributions in the slab (medium 2) and in the two half-spaces of host material (free space in this case) for $z < -h$ (medium 1) and $z > 0$ (medium 3) can be expressed as the superpositions of incident and reflected waves:

$$V_i(z) = V_i^+ e^{-jkiz} + V_i^- e^{jkiz}, \quad (18)$$

where the subscript $i = 1, 2, 3$ indicates the portion of space under consideration. The propagation constant and the characteristic impedance of the transmission lines in Figure 11 are those of the host material for medium 1 and 3 and those of SC material for medium 2.

After a few algebraic steps, the transmission line solution for the value of the voltage propagating after the slab to the receiver of the measurement setup is

$$V_3^+ = V_2^+ (1 + \Gamma_{\text{out}}) = V_1^+ \frac{e^{jk_1 h} (1 + \Gamma_{\text{in}})(1 + \Gamma_{\text{out}})}{e^{jk_2 h} + \Gamma_{\text{out}} e^{-jk_2 h}}, \quad (19)$$

where $\Gamma_{\text{in}} = (Z_{\text{in}2} - \zeta_{\text{host}})/(Z_{\text{in}2} + \zeta_{\text{host}})$ and $\Gamma_{\text{out}} = (\zeta_{\text{host}} - \zeta)/(\zeta_{\text{host}} + \zeta)$ are the voltage reflection coefficients at the cross sections $z = -h$ and $z = 0$, respectively.

Figure 12 presents the amplitude of the transmission coefficient $T = V_3^+/V_1^+$ as a function of the frequency for a dielectric slab of Si of thickness $h = 434 \mu\text{m}$ and resistivity declared by the provider of $5 \Omega\text{cm}$. The value of $\epsilon_{r,\infty}$ of the slab was found beforehand to be 10.5. In the model, a nominal resistivity of $\rho_{qs} = 3.77 \Omega\text{cm}$ corresponding to a doping of $n = 1.16 \times 10^{21}$ was adopted because it led to the best fit. The scattering time was found using (7). It is apparent that the frequency-independent nominal resistivity, or conductivity, does not represent the losses in the dielectric slab for frequencies higher than a few hundred GHz.

Meanwhile, the transmission coefficient evaluated via the full Drude model and the measured one show very good agreement in measurement accuracy. The expected and measured oscillations are directly related to the multiple reflections at the dielectric air interfaces.

From the same measurements, the TDS measurement equipment [20] allows for the extraction of the index of refraction, $(\sqrt{\epsilon_{r,\text{eff}}})$. In Figure 13, the measured real and imaginary parts (red solid curves) are compared with the ones predicted by the Drude model (black solid lines) and with those from a model that only considers the quasi-static, frequency-independent approximation for the conductivity (dashed lines). It is apparent that the accuracy of the measured $\text{Im}\{\sqrt{\epsilon_{r,\text{eff}}}\}$ (proportional to the attenuation constant) is impacted by the multiple reflections within the slab. On the large scale of Figure 13(a), both models seem to agree very well with measurements. However, Figure 13(b)–(d) shows expanded views of the imaginary part of the index of refraction on separate frequency ranges. The larger apparent dispersions occur at lower frequencies, with $\text{Im}\{\sqrt{\epsilon_{r,\text{eff}}}\}$ varying from -0.7 to -0.1 in the band, from 100 GHz to 500 GHz. However, in that frequency range, the quasi-static approximation of the conductivity already provides $\text{Im}\{\sqrt{\epsilon_{r,\text{eff}}}\}$ with good accuracy with respect to the measurements and the Drude model. In the frequency range between 0.5 THz and 1.5 THz, the measured $\text{Im}\{\sqrt{\epsilon_{r,\text{eff}}}\}$ and the one predicted by the Drude model start to significantly deviate from the one predicted by the quasi-static conductivity model. Finally, in the ranges from 1.5 THz to 4 THz, the $\text{Im}\{\sqrt{\epsilon_{r,\text{eff}}}\}$ is five to 20 times smaller than the one predicted

by the quasi-static conductance approximation, indicating that the full Drude model must be used to assess the losses in doped SCs to maintain a useful estimation of the propagation losses. Overall, the Drude model captures the dominant features very well, validating the analysis from the previous sections.

APPLICATIONS IN ABSORBERS AND LENS DESIGN

In the “Drude Model Predictions” section, integrated lens arrays for imagers were introduced as a typical field of applications where the Drude model is commonly overlooked while estimating losses. In this section, numerical examples will be described to highlight the usefulness of adopting the Drude model in the design stages of integrated-lens antennas and absorber design.

In the previous section, it was presented that the transmission line model from Figure 11 can be used to estimate the power absorbed in a slab of finite thickness which is surrounded by free space. Here, we will consider a slab of doped Si embedded in both nondoped Si and free space as examples. The absorbed power in the slab can be expressed as

$$P_{\text{abs}} = \frac{1}{2} \iiint_{V_{\text{SC}}} \text{Re}\{\sigma\} |\vec{E}_2(x, y, z)|^2 dV, \quad (20)$$

where V_{SC} is the volume of the SC slab, and \vec{E}_2 is the electric field inside the slab. The integral can be analytically evaluated as

$$P_{\text{abs}} = \frac{\text{Re}\{\sigma\} A}{2} |V_2^+|^2 \frac{1}{2\alpha} (e^{2\alpha h} - 1 + |\Gamma_{\text{out}}|^2 (1 - e^{-2\alpha h})), \quad (21)$$

where σ is provided in (3), $\alpha = -\text{Im}\{k_2\}$, and A is the effective area under illumination. The effective area under illumination is only needed to provide absolute power values. However, if the absorbed power is normalized to the incident power,

$$P_{\text{inc}} = \frac{1}{2} \frac{A}{\zeta_{\text{host}}} |V_1^+|^2, \quad (22)$$

the effective area information cancels out.

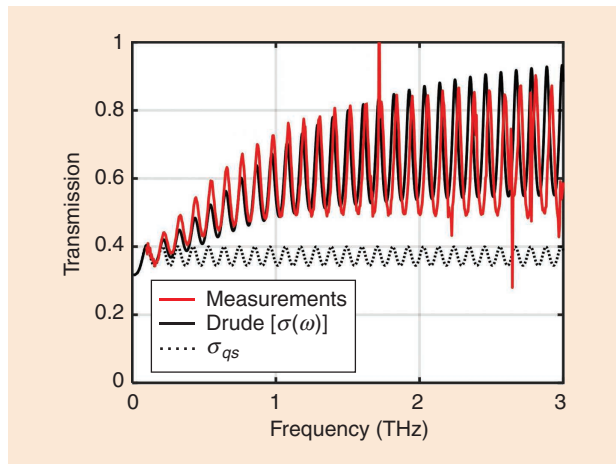


FIGURE 12. The transmission through a slab of doped Si ($h = 434 \mu\text{m}$; $n = 1.16 \times 10^{21} \text{m}^{-3}$) and a comparison between the measurements of the Drude model and of the quasi-static approximation.

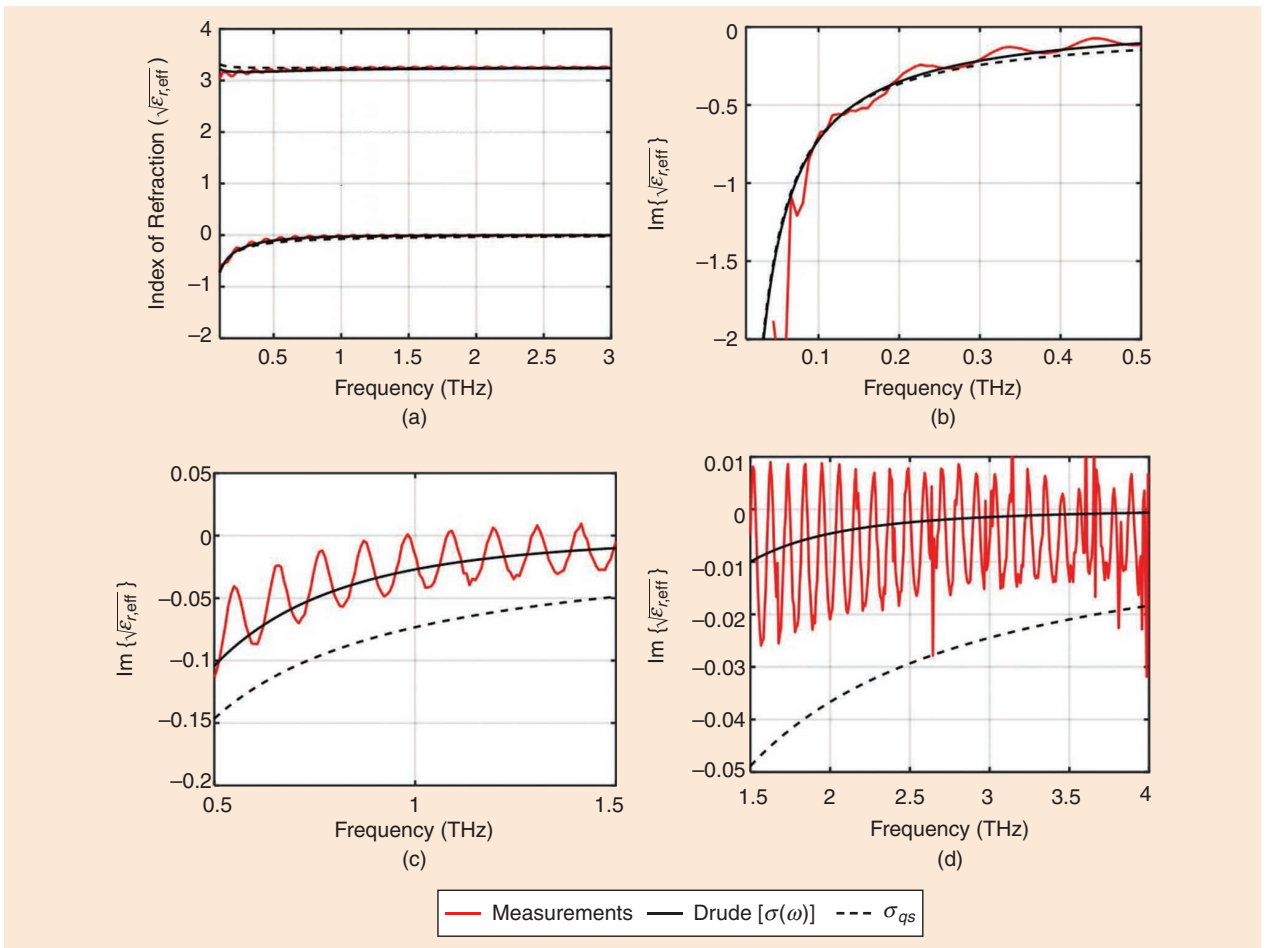


FIGURE 13. The index of refraction of the Si slab with $h = 434 \mu\text{m}$ and $n = 1.16 \times 10^{21} \text{m}^{-3}$. (a) Wide frequency range. (b)–(d) Zoomed on specific frequency regions.

ABSORBING SLAB SURROUNDED BY SILICON

Using the transmission line model from Figure 11 and (21) and (22), one can calculate the losses associated to the low-resistive Si layer in the front-end design introduced in

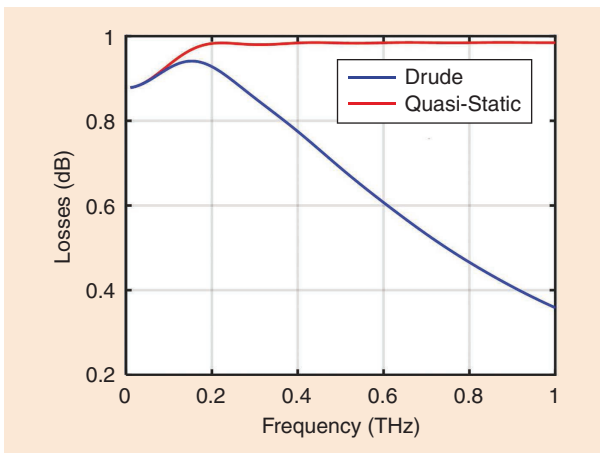


FIGURE 14. The losses in a slab of $200 \mu\text{m}$ with $\rho_{qs} = 10 \Omega\text{cm}$ ($n = 4.5 \times 10^{20} \text{m}^{-3}$). The expected losses are displayed as calculated (using the quasi-static approximation and the Drude model).

Figure 1 [14]. The frequency band under consideration is from 200 to 600 GHz, the thickness of the slab is $200 \mu\text{m}$, and the quasi-static resistivity is $10 \Omega\text{cm}$. This resistivity corresponds to a doping level of $n = 4.5 \times 10^{20} \text{m}^{-3}$. From the quasi-static approximation, the expected losses over the frequency band of interest are constantly slightly below 1 dB. However, after implementing the Drude model, it is seen that the losses actually peak at 200 GHz at 1 dB before decreasing with frequency to only 0.6 dB at 600 GHz and even lower at higher frequencies. The losses as a function of frequency, calculated using both models, are displayed in Figure 14. From Figure 14 it is clear that the commonly used quasi-static approximation for the conductivity severely overestimates the losses at higher frequencies for the transmission of a wave through low-resistive Si. The lower losses, as calculated from the Drude model, show greater promise for the integration of antennas in low-resistive Si just below Si lenses at THz frequencies.

The doping level can be tuned to maximize absorption: The highest absorbing efficiency is achieved by the thinnest slab that absorbs the maximum power for a given frequency. Assuming a frequency band is centered around a given central frequency, such an SC absorber can be synthesized parametrically by

tuning the electron doping, n , and the thickness, h . A good absorber will be one that

- 1) minimizes the reflections of the incident waves, i.e., one for which $\zeta_{SC} \approx \zeta_{host}$
- 2) maximizes resistive wave attenuation.

As previously introduced, three frequency regimes, $f < f_\tau$, $f_\tau < f < f_p$, and $f > f_p$, can be identified from the Drude model. For frequencies below f_p , the real part of the effective dielectric constant is smaller than zero. For frequencies that are also lower than f_τ , waves can still propagate in the SC, with the attenuation constant equal to the propagation constant. However, for frequencies in the range of $f_\tau < f < f_p$, there is no propagation possible, with or without attenuation. Accordingly, the frequencies between f_τ and f_p are less useful for an efficient absorber. It is apparent that for SC absorbers f_p is a design parameter since the doping n can be finely tuned in a cleanroom environment. Accordingly, a starting point for our SC absorber design will be the choice of an electron density doping that cuts out the middle frequencies' region, which is achieved by choosing $n = n_p$.

Looking at the absorption within slabs of different thicknesses, as presented in Figure 15, it is apparent that for $n = n_p$ a slab with a thickness of one effective wavelength at 350 GHz, corresponding to approximately $250 \mu\text{m}$, is sufficient to absorb more than 90% of the incident power. As expected, thicker and thinner slabs absorb a larger and smaller portion of the incident power, respectively. Figure 16 illustrates the power absorbed by a slab of thickness $h = 250 \mu\text{m}$ as a function of the frequency and doping level. Lower dopings lead to lower impedance contrasts, associated to a lower X_{Si} . On one hand, this also implies lower ohmic attenuations. On the other hand, higher dopings lead to a higher attenuation per unit length but also higher reflection at the interfaces.

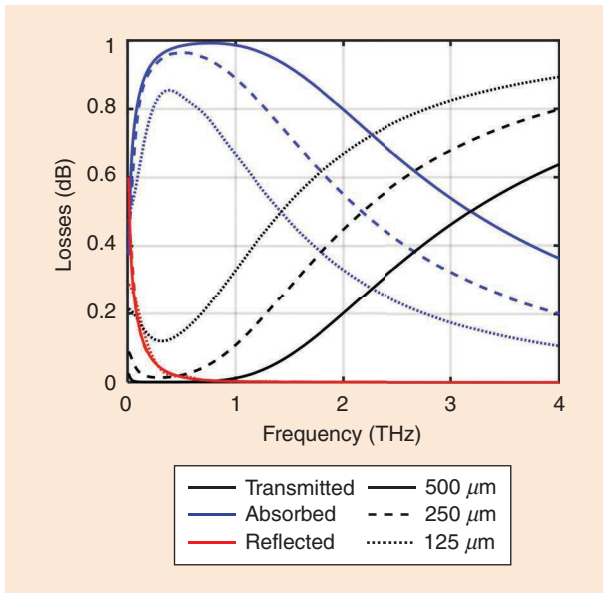


FIGURE 15. The calculated, normalized transmitted absorbed and reflected power in a doped Si slab ($n = n_p = 8.8 \times 10^{21}$, $\rho = 0.6 \Omega\text{cm}$), surrounded by nondoped Si. Three different slab heights are considered.

ABSORBING SLAB SURROUNDED BY FREE SPACE

A clearer example of the usefulness of the transmission line representation for the propagation in SC material involves minimizing the volume of an SC stratification to absorb a wave incident from free space. In this case, an Si with the higher doping level $n = 6n_p = 5.3 \times 10^{22} \text{ m}^{-3}$ was chosen for the main absorber. The power absorbed in this single slab absorber (of thickness $125 \mu\text{m}$) is presented in Figure 17,

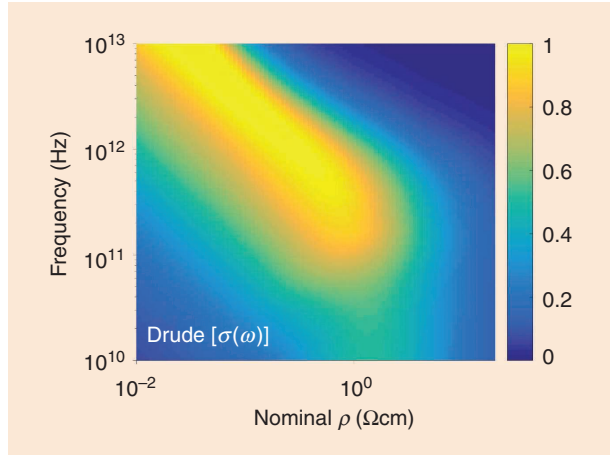


FIGURE 16. The normalized absorbed power in a slab of doped Si, $h = 250 \mu\text{m}$, as a function of both the doping and the frequency calculated using the Drude model.

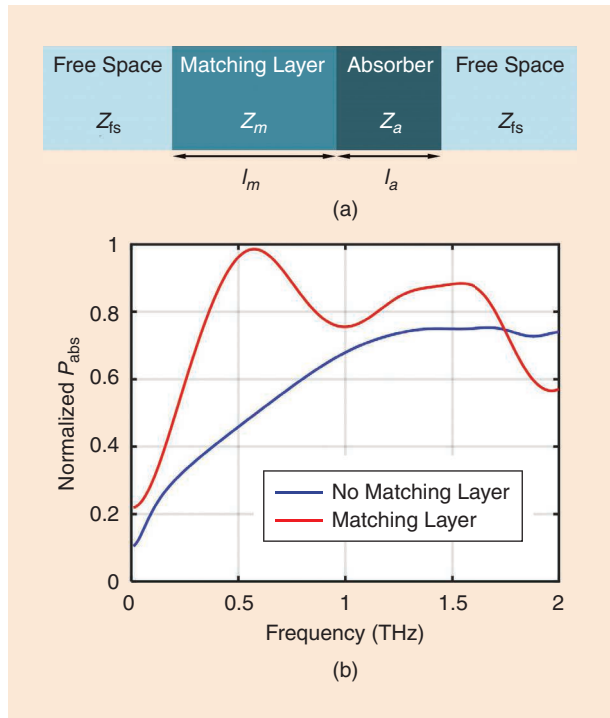


FIGURE 17. (a) A densely doped Si absorber with a matching layer surrounded by free space. (b) Absorbed power in the structure normalized to total incident power for the cases with ($l_m = 81 \mu\text{m}$, $l_a = 44 \mu\text{m}$) and without a matching layer ($l_a = 125 \mu\text{m}$). The remaining parameters are $n = 6n_p = 5.3 \times 10^{22} \text{ m}^{-3}$ and $\epsilon_{r,m} = 3.4$, $n_m = 3 \times 10^{21} \text{ m}^{-3}$.

with the maximum absorption being 75% around 1.5 THz. However, the introduction of a second perforated doped-Si matching layer can be used to facilitate the penetration from free space to the densely doped Si. The effective dielectric permittivity of the matching layer in the absence of doping is $\epsilon_{r,m} = \sqrt{\epsilon_{r,oc}} = 3.4$. In this second case, the matching layer was taken with $l_m = 81 \mu\text{m} = \lambda_d/4$ at 500 GHz, where λ_d is the wavelength in the matching layer. The thickness of the core absorber was reduced to $l_a = 44 \mu\text{m}$ so that the total absorbing thickness remained $125 \mu\text{m}$. The doping level of the matching layer was chosen to be $n_m = 3 \times 10^{21} \text{m}^{-3}$. In this second case, more than 95% of the power was absorbed in the cumulative space of $\lambda_0/5$ at 500 GHz. It was interesting to observe that, despite the heavy losses in the matching layer, the standard quarter wavelength transformation rule still roughly applied.

CONCLUSIONS

The frequency-dependent properties of gold and doped Si were investigated using the Drude model. The propagation constant of bulk Si for different levels of n-type dopings was presented. The characteristic impedance for low-resistivity Si was also introduced and used in a classic transmission line tool. Here, the notable feature is that this tool is used as it is in standard microwave designs, also in the presence of very high losses per wavelength. The model was validated by means of time-domain sensing measurements. It was found that the commonly used quasi-static approximation for the conductivity is valid for frequency regimes up to a few hundred GHz. However, for frequencies higher than 300 GHz, the Drude model exhibits significantly more accurate results than the quasi-static model when measurements are compared.

Guidelines were presented for synthesizing efficient THz absorbers for a given target frequency by finely tuning the doping of semiconducting materials. By introducing a matching layer, an absorption of more than 95% of the incident power is realized in a slab of $1/5$ of the wavelength in free space. As the frequency increases above the target frequency, the absorption decreases, and the losses in the doped Si are much lower than would be assumed from the quasi-static conductance model.

AUTHOR INFORMATION

Ralph M. van Schelven (r.m.vanschelven@tudelft.nl) is with the Microelectronics Department, THz Sensing Group, Delft University of Technology, Mekelweg 4, 2628 CD, Delft, The Netherlands, where he is a Ph.D. candidate. He is a Student Member of IEEE.

Arturo Fiorellini Bernardis (a.fiorellinibernardis@tudelft.nl) is with the Microelectronics Department, THz Sensing Group, Delft University of Technology, Mekelweg 4, 2628 CD, Delft, The Netherlands, where he is a Ph.D. candidate. His research interests include electromagnetic theory and photoconductive antennas.

Paolo Sberna (p.m.sberna@tudelft.nl) is with the Microelectronics Department, THz Sensing Group, Delft

University of Technology, Mekelweg 4, 2628 CD, Delft, The Netherlands.

Andrea Neto (a.neto@tudelft.nl) is with the Microelectronics Department, THz Sensing Group, Delft University of Technology, Mekelweg 4, 2628 CD, Delft, The Netherlands. His research interests include the analysis and design of antennas. He is a Fellow of IEEE.

REFERENCES

- [1] P. Drude, "Zur Elektronentheorie der Metalle," *Annalen der Physik*, vol. 306, no. 3, pp. 566–613, Mar. 1900. doi: 10.1002/andp.19003060312.
- [2] M. A. Leontovich, "Approximate boundary conditions for electromagnetic fields at the surface of a highly conducting body," *Issledovaniyapo Rasprostraneniyu Radiovoln, Moscow*, vol. 2, pp. 5–12, 1948.
- [3] K. S. Champlin, D. B. Armstrong, and P. D. Gunderson, "Charge carrier inertia in semiconductors," *Proc. IEEE*, vol. 52, no. 6, pp. 677–685, 1964. doi: 10.1109/PROC.1964.3049.
- [4] L. E. Dickens, "Spreading resistance as a function of frequency," *IEEE Trans. Microw. Theory Techn.*, vol. 15, no. 2, pp. 101–109, Feb. 1967. doi: 10.1109/TMTT.1967.1126383.
- [5] K. S. Champlin and G. Eisenstein, "Cutoff frequency of submillimeter Schottky-barrier diodes," *IEEE Trans. Microw. Theory Techn.*, vol. 26, no. 1, pp. 31–34, 1978. doi: 10.1109/TMTT.1978.1129302.
- [6] M. van Exter and D. Grischkowsky, "Carrier dynamics of electrons and holes in moderately doped silicon," *Phys. Rev. B*, vol. 41, no. 17, pp. 12,140–12,149, June 1990. doi: 10.1103/PhysRevB.41.12140.
- [7] T.-I. Jeon and D. Grischkowsky, "Characterization of optically dense, doped semiconductors by reflection THz time domain spectroscopy," *Appl. Phys. Lett.*, vol. 72, no. 23, June 8, 1998. doi: 10.1063/1.121531.
- [8] S. Nashima, O. Morikawa, K. Takata, and M. Hangyo, "Measurement of optical properties of highly doped silicon by terahertz time domain reflection spectroscopy," *Appl. Phys. Lett.*, vol. 79, no. 24, pp. 3923–3925, 2001. doi: 10.1063/1.1413498.
- [9] M. Dressel and G. Grüner, *Electrodynamics of Solids: Optical Properties of Electrons in Matter*. Cambridge, U.K.: Cambridge Univ. Press, 2002.
- [10] M. Dressel and M. Scheffler, "Verifying the Drude response," *Annalen der Physik*, vol. 15, no. 7–8, pp. 535–544, 2006. doi: 10.1002/andp.200510198.
- [11] K. J. Willis, S. C. Hagness, and I. Knezevic, "A generalized Drude model for doped silicon at terahertz frequencies derived from microscopic transport simulation," *Appl. Phys. Lett.*, vol. 102, no. 12, p. 122,113, 2013. doi: 10.1063/1.4798658.
- [12] R. Al Hadi et al., "A 1 k-pixel video camera for 0.7–1.1 terahertz imaging applications in 65-nm CMOS," *IEEE J. Solid-State Circuits*, vol. 47, no. 12, pp. 2999–3012, Dec. 2012. doi: 10.1109/JSSC.2012.2217851.
- [13] J. Grzyb, K. Statnikov, N. Sarmah, B. Heinemann, and U. R. Pfeiffer, "A 210–270-GHz circularly polarized FMCW radar with a single-lens-coupled SiGe HBT chip," *IEEE Trans. Terahertz Sci. Technol.*, vol. 6, no. 6, pp. 771–783, Nov. 2016.
- [14] S. L. van Berkel et al., "Wideband double leaky slot lens antennas in CMOS technology at sub-millimeter wavelengths," *IEEE Trans. Terahertz Sci. Technol.*, vol. 10, no. 5, pp. 540–553, July 2020.
- [15] S. J. C. Yates et al., "Surface wave control for large arrays of microwave kinetic inductance detectors," *IEEE Trans. THz Sci. Technol.*, vol. 7, no. 6, pp. 789–799, Nov. 2017. doi: 10.1109/TTHZ.2017.2755500.
- [16] S. van Berkel, O. Yurduseven, A. Freni, A. Neto, and N. Llombart, "THz imaging using uncooled wideband direct detection focal plane arrays," *IEEE Trans. THz Sci. Technol.*, vol. 7, no. 5, pp. 481–492, Sept. 2017. doi: 10.1109/TTHZ.2017.2736338.
- [17] S. Bosma, M. Alonso-delPino, C. Jung-Kubiak, D. Blanco, and N. Llombart, "Scanning lens phased array for submillimeter wavelengths," in *Proc. IRMMW*, Paris, 2019, pp. 1–2.
- [18] S. Ramo, J. R. Whinnery, and T. V. Duzer, *Fields and Waves in Communication Electronics*. Hoboken, NJ: Wiley, 1990.
- [19] D. B. M. Klaasen, "A unified mobility model for device simulation – I. Model equations and concentration dependence," *Solid State Electron.*, vol. 35, no. 7, pp. 953–959, 1992.
- [20] "TERA K15 all fiber-coupled terahertz spectrometer," Menlo Systems. <https://www.menlosystems.com/products/thz-time-domain-solutions/terak15-terahertz-spectrometer/>

